curate photometric and geometric calibration and intercomparison of the atmospheric experiment results will provide the strongest possible constraints on atmospheric properties, even for regions of the planet not affected by the impacts. Collaborations with other observers will also fill in spectral, spatial, and temporal gaps in coverage. These data will be used to refine models of the jovian system, particularly the atmosphere, and will be used to support the interpretation of observations made by the Galileo mission at Jupiter.

REFERENCES AND NOTES

1. Selection of science goals was made by science team members M. A'Hearn, K. Baines, D. Deming, T. Dowling, C. Griffith, J. Goguen, H. Hammel, W. Hoffmann, D. Hunten, D. Jewitt, T. Kostiuk, S. Miller, K. Noll, G. Orton (chair), and K. Zahnle.
2. These include atmospheric inertia-gravity waves [J. Harrington, R. P. LeBeau, K. A. Backes, T. E. Dowling, *Nature* **368**, 525 (1994)], internal seismic waves [M. Marley, *Astrophys. J. Lett.* **427**, L63 (1994); found with a search method presented in D. H. Hunten, W. F. Hoffmann, A. L. Sprague, *Geophys. Res. Lett.* **1**, 1091 (1994)], and trapped oscillations (*p*-modes) induced by the collisions. We will report on these investigations elsewhere.
3. J. Rayner *et al.*, *Proc. SPIE* **1946**, 490 (1993).
4. T. Greene, A. T. Tokunaga, D. W. Toomey, J. S. Carr, *ibid.*, p. 313. Both NSFCAM and CSHELL are IRTF facility instruments that used 256 by 256 detector arrays.
5. W. F. Hoffmann, G. G. Fazio, K. Shivanandan, J. L. Hora, L. K. Deutsch, *Proc. SPIE* **1946**, 449 (1993); *Infrared Phys. Technol.* **35**, 175 (1994). MIRAC2 was constructed and is operated by Steward Observatory, University of Arizona, and the Smithsonian Astrophysical Observatory. It was commissioned on 13 July 1994 with a 128 by 128 detector Si:As array, which was used between 2 and 21 μm.
6. J. Lacy *et al.*, *Publ. Astron. Soc. Pac.* **101**, 1166 (1989). IRSHELL is operated by the University of Texas at Austin. A 20 by 64 detector array in IRSHELL, used between 7 and 17 μm, was first used on 19 July.
7. T. Kostiuk and M. J. Mumma, *Appl. Opt.* **22**, 2644 (1983); T. Kostiuk, *Infrared Phys. Technol.* **35**, 243 (1994). Both the IRHS technique and its application to planetary atmospheric studies are described in these papers. The IRHS is capable of measuring the shapes of spectroscopic lines emitted by Jupiter's stratosphere.
8. D. Jewitt and P. Kalas, communication posted to the Shoemaker-Levy 9 electronic bulletin board (Planetary Data System Small Bodies Node, University of Maryland), 19 July 1994.
9. H. B. Hammel *et al.*, *Science* **267**, 1288 (1995).
10. J. R. Graham, I. De Pater, J. Garrett Jernigan, M. C. Liu, M. E. Brown, *ibid.*, p. 1320; P. D. Nicholson *et al.*, *Geophys. Res. Lett.*, in press. The arrival times of the first signals detected by the Palomar and Keck telescopes agree to within 7 s.
11. G. S. Orton *et al.*, *Science* **252**, 537 (1991); G. S. Orton *et al.*, *ibid.* **265**, 625 (1994).
12. M. Flasar, in *Time-Variable Phenomena in the Jovian System*, M. Belton, G. Hunt, R. West, Eds. (NASA Spec. Publ. 494, National Aeronautics and Space Administration, Washington, DC, 1986), p. 324.
13. G. Orton, J. Lacy, A. Castillo, J. Achtermann, P. Parmar, *Bull. Am. Astron. Soc.* **24**, 1041 (1992).
14. T. Kostiuk, F. Espenak, M. J. Mumma, D. Deming, D. Zipoy, *Icarus* **72**, 394 (1987); T. Livengood, T. Kostiuk, F. Espenak, J. Goldstein, *J. Geophys. Res.* **98**, 18813 (1993).
15. The temperature near 1 μbar was determined to be 200 ± 50 K from the Voyager 2 Ultraviolet Spectrometer α Leo occultation experiment [S. K. Atreya, T. Donahue, M. C. Festou, *Astrophys. J.* **247**, L43 (1981); M. C. Festou *et al.*, *J. Geophys. Res.* **86**, 5715 (1981)].
16. R. West *et al.*, *Science* **267**, 1296 (1995).
17. P. J. Gierasch, B. J. Conrath, J. A. Magalhaes, *Icarus* **67**, 456 (1986).
18. P. Drossart *et al.*, *Nature* **340**, 539 (1989).
19. S. Miller *et al.*, *Geophys. Res. Lett.*, in press.
20. S. J. Kim, *Icarus* **75**, 399 (1988); J. Caldwell, A. T. Tokunaga, G. S. Orton, *ibid.* **53**, 133 (1983).

21. We thank the engineering staff of the IRTF, headed by P. Jensen, for their support in making so many late improvements to the telescope performance possible. This research was sponsored by various grants from NASA and NSF for work performed at each of the institutions with which the authors of this paper are associated. The MIRAC2 upgrade to the 128 × 128 array was also supported by Steward Observatory, University of Arizona, and Smithsonian Astrophysical Observatory. T.L. was a National Research Council Resident Research Associate. M.A'H., K.B., A.D., L.D., F.E., P.E., K.F., J.F., J. Goguen, C.G., H.H., J. Harrington, W.H., J. Hora, D.H., D.K., R.K., T. Kostiuk, J.L., C.L., S.M., K.N., G.O., A.S., K.W., P.Y.-F., K.Z., and D.Z. were visiting astronomers at IRTF, which is operated by the University of Hawaii under contract to NASA. We thank Research Systems, Inc., for donating several licenses for the Interactive Data Language (IDL), which was used to generate most of the graphics in this paper. B. Taylor is gratefully acknowledged for data reduction support, as are C. Lachata and S. Benskin for color photographic services.

The Hubble Space Telescope (HST) Observing Campaign on Comet Shoemaker-Levy 9

H. A. Weaver,* M. F. A'Hearn, C. Arpigny, D. C. Boice, P. D. Feldman, S. M. Larson, P. Lamy, D. H. Levy, B. G. Marsden, K. J. Meech, K. S. Noll, J. V. Scotti, Z. Sekanina, C. S. Shoemaker, E. M. Shoemaker, T. E. Smith, S. A. Stern, A. D. Storrs, J. T. Trauger, D. K. Yeomans, B. Zellner

The Hubble Space Telescope made systematic observations of the split comet P/Shoemaker-Levy 9 (SL9) (P designates a periodic comet) starting in July 1993 and continuing through mid-July 1994 when the fragments plunged into Jupiter's atmosphere. Deconvolutions of Wide Field Planetary Camera images indicate that the diameters of some fragments may have been as large as ~2 to 4 kilometers, assuming a geometric albedo of 4 percent, but significantly smaller values (that is, <1 kilometer) cannot be ruled out. Most of the fragments (or nuclei) were embedded in circularly symmetric inner comae from July 1993 until late June 1994, implying that there was continuous, but weak, cometary activity. At least a few nuclei fragmented into separate, condensed objects well after the breakup of the SL9 parent body, which argues against the hypothesis that the SL9 fragments were swarms of debris with no dominant, central bodies. Spectroscopic observations taken on 14 July 1994 showed an outburst in magnesium ion emission that was followed closely by a threefold increase in continuum emission, which may have been caused by the electrostatic charging and subsequent explosion of dust as the comet passed from interplanetary space into the jovian magnetosphere. No OH emission was detected, but the derived upper limit on the H_2O production rate of $\sim 10^{27}$ molecules per second does not necessarily imply that the object was water-poor.

The Hubble Space Telescope (HST) first observed the periodic comet SL9 on 1 July 1993 (*1*). After the successful HST servicing mission in December 1993, the HST began observing SL9 again in January 1994 and monitored the comet until its impact into Jupiter in mid-July (Table 1).

Because of the large spatial extent of SL9 in 1994 and the relatively small fields of view of the HST cameras, the only time that the HST observed the entire "train" of fragments during 1994 was on 17 May. Figure 1 shows the composite SL9 image created from some images taken on this date with the Wide Field Planetary Camera 2 (WFPC2) (*2*) and identifies the fragments with their letter labels. Fragment A was the first to impact Jupiter (on 16 July 1994) and nucleus W was the last (on 22 July 1994). The apparent separation of fragments A and W increased by a factor of ~5 (from 70 to 360 arc sec) between the time of the first HST images taken on 1 July 1993 and the ones taken on 17 May 1994.

Although a total of 39 orbits of HST observing time was devoted to imaging of the comet (*3*), this was not nearly enough to provide detailed temporal coverage on all the fragments. We focused our attention on three different portions of SL9: the regions around the complex of fragments P and Q, the S fragment, and the G fragment. All of

Fig. 1. A mosaic of comet SL9 compiled from six separate images taken with the HST WFPC2 in wide-field mode on 17 May 1994. Each fragment is labeled with its letter designation. The apparent separation of A and W was ~360 arc sec, corresponding to a projected distance at SL9 of 1.15×10^6 km. The regions near the brighter fragments are strongly saturated in this figure in order to improve the visibility of the fainter fragments. The compass gives the directions of celestial north (N) and celestial east (E). The scale bar indicates arc seconds.

the latter fields contained bright fragments. The P-Q and S regions showed particularly interesting morphologies, whereas the G region appeared to be a good example of a relatively isolated bright fragment.

Image Analysis

Figure 2 shows the temporal evolution of the P-Q complex during the entire period of the HST observations. Fragments Q1 and Q2 clearly seem to have split off from a common parent. An analysis of their orbits indicates that the breakup occurred during April 1993 (*4*).

Several other fragments also showed signs of splitting well after the tidal disruption of the SL9 parent body in July 1992. The image of P2 was clearly elongated on 24 January 1994 and had two distinct components by 30 March 1994 (Fig. 2). A small companion to the G fragment was observed in ground-based (*5*) and HST observations in May 1994 (Fig. 1). Such fragmentation events can be explained quite naturally as the splitting of single, coherent bodies that are located near the centers of each of the comae in SL9. It seems implausible that a swarm of debris (or a "traveling sandbank," to use the terminology from the classical literature on comets) would break up into separate discrete clumps. Clearly, these SL9 nuclei were very fragile, which is consistent with other observations of cometary nuclei.

As shown in Figs. 2 and 3, the comae were nearly circular within ~2000 km of each fragment until about 2 weeks before impact with Jupiter, at which time the comae became highly elongated approximately along the direction of motion. This accelerated stretching near the time of impact was presumably due to the acceleration deep in the jovian gravitational field, but we have not attempted to model the coma shape in detail. Despite this stretching, the brightness of the cores remained strongly peaked spatially with no evidence for catastrophic fragmentation through the final observations, the latest of which were taken ~10 hours before impact (*6*).

The inner comae remained circular even as the SL9 train length increased by a factor of ~10. If the circularly symmetric inner comae were composed of large dust particles that were essentially unaffected by solar radiation pressure and, thus, were in orbits similar to those of their parent nuclei (*1*), we would expect these comae to be stretched along the direction of the train in a manner similar to that observed for the train itself, but such a tendency was not observed. A spherical cloud of large particles could possibly maintain its symmetry over long periods if the dust velocities were very small (on the order of ~5 cm s^{-1} or smaller) and isotropic relative to the parent nucleus (*7*).

Another possible explanation for the circular coma is that each fragment was pro-

H. A. Weaver, K. S. Noll, T. E. Smith, and A. D. Storrs are with the Space Telescope Science Institute, Baltimore, MD 21218, USA. M. F. A'Hearn is in the Department of Astronomy, University of Maryland, College Park, MD 20742, USA. C. Arpigny is with the Université de Liège, Institut d'Astrophysique, B-4000 Liège, Belgium. D. C. Boice is with the Southwest Research Institute, Division 15, 6220 Culebra Road, San Antonio, TX 78228, USA. P. D. Feldman is in the Department of Physics and Astronomy, Johns Hopkins University, Baltimore, MD 21218, USA. S. M. Larson, D. H. Levy, and J. V. Scotti are with the Lunar and Planetary Laboratory, University of Arizona, Tucson, AZ 85721, USA. P. Lamy is with the Laboratorie d'Astronomie Spatiale, BP 8, 13376 Marseille, Cedex, 12 France. B. G. Marsden is with the Harvard-Smithsonian Center for Astrophysics, Cambridge, MA 02138, USA. K. J. Meech is with the University of Hawaii, Institute for Astronomy, 2680 Woodlawn Drive, Honolulu, HI 96822, USA. Z. Sekanina, T. J. Trauger, and D. K. Yeomans are with the Jet Propulsion Laboratory, Pasadena, CA 91109, USA. C. S. Shoemaker is in the Department of Physics and Astronomy, Northern Arizona University, Flagstaff, AZ 86011, USA. E. M. Shoemaker is with the U.S. Geological Survey, 2255 North Gemini Drive, Flagstaff, AZ 86001, USA. S. A. Stern is with the Southwest Research Institute, Division 15, Boulder Extension Office, 1050 Walnut Street, Boulder, CO 80302, USA. B. Zellner is in the Department of Physics, Georgia Southern University, Statesboro, GA 30460, USA.

*To whom correspondence should be addressed.

Table 1. Log of HST observations of SL9. Orbit refers to the natural accounting unit that is often used for HST observing time. The HST orbital period is ~96 min, but the Earth occults the target for ~42 min each orbit. Thus, the target has a visibility window of ~54 min during each orbit, of which ~24 min is devoted to spacecraft and instrument overhead. A total of 39 HST orbits were used for WFPC imaging of SL9 and 78 images were obtained. A total of six HST orbits were devoted to Faint Object Spectrograph (FOS) spectroscopy of SL9 with total exposure time of 171 min. The geocentric distance is the Earth-SL9 distance in astronomical units (AU). The sun-SL9 distance was ~5.4 AU for the entire period of HST observations. The phase angle is the Earth-SL9-sun angle. UT, universal time.

Date (UT)	Instrument	No. of orbits	Geocentric distance (AU)	Phase angle (degrees)
1 July 1993	WFPC1, FOS	2, 1	5.5	10.7
24–27 January 1994	WFPC2	10	5.4	10.5
28–30 March 1994	WFPC2, FOS	6, 3	4.5	5.8
17 May 1994	WFPC2	3	4.4	3.7
23–27 June 1994	WFPC2	7	4.8	9.4
4 July 1994	WFPC2	1	4.9	10.0
11 July 1994	WFPC2	2	5.0	10.4
14 July 1994	WFPC2, FOS	4, 2	5.1	10.5
18–20 July 1994	WFPC2	5	5.2	10.7

ducing dust continuously like a typical comet (8). The inner coma brightness profile is approximately inversely proportional to the projected distance from the fragment (Fig. 3), a brightness profile expected for steady-state dust production. Using conventional assumptions for the dust properties (9), we calculated that a dust production rate of ~5 kg s^{-1} is needed to match the observed spatial profile near the brighter fragments, which is ~1/10 the rate derived for P/Schwassmann-Wachmann 1 at a heliocentric distance of 5.8 astronomical units (AU) (*10*) and comparable to the rate derived for P/Halley at a heliocentric distance of 4.8 AU pre-perihelion (*11*).

The momentum impulse from this dust production on the sunlit hemispheres of the fragments might cause significant nongravitational orbital perturbations for small bodies (that is, those having a mass of $\lesssim 10^{14}$ g), perhaps explaining (*12*) why some of the fragments in SL9 were significantly displaced from the "train." However, we have successfully modeled the relative separations of Q1 and Q2 without using these nongravitational perturbations and are investigating whether splitting events could account for the positions of the other off-train fragments.

Sizes of the Nuclei

Because the energy deposited into Jupiter's atmosphere by the SL9 fragments was proportional to the cube of their size, putting constraints on the latter was the most important goal of our program. We performed detailed analyses of the spatial brightness distributions near most of the fragments to determine how much of the core brightness might be due to an unresolved fragment and how much was due to the coma. Only the highest resolution images (those taken by WFPC2 in planetary mode) were used for these analyses.

The resolution of the WFPC2 in planetary mode was ~250 km at SL9, too large to resolve the fragments, but we had hoped to find clear evidence for an unresolved source (that is, a feature whose light distribution was indistinguishable from the point spread function of the camera) on top of a well-defined coma brightness distribution. Unfortunately, this was not the case, as Fig. 3 shows. The steep inner coma brightness distribution cannot be fit adequately by a single power law profile; the coma must contribute a significant fraction of the light observed in the brightest pixel, but a deter-

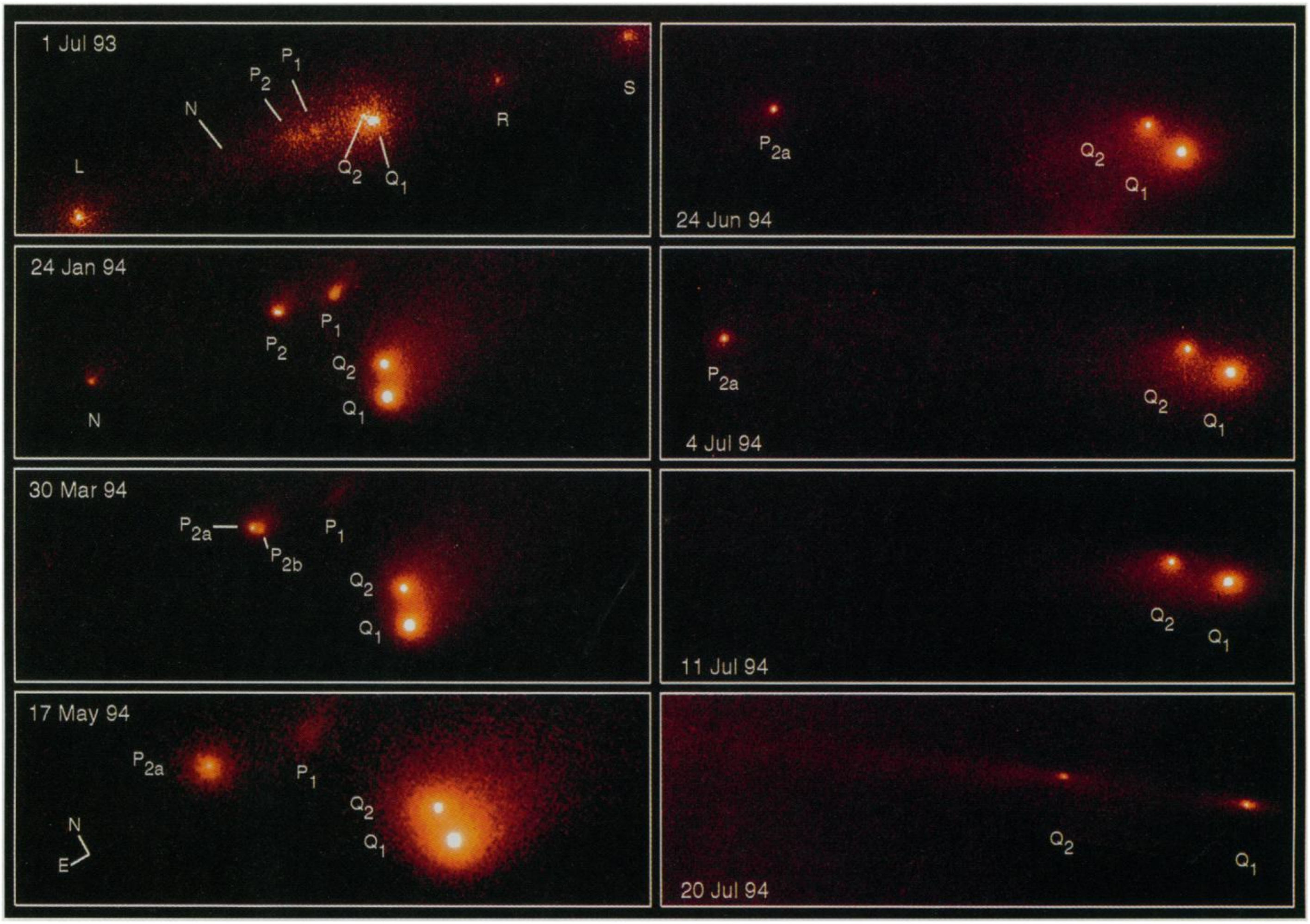

Fig. 2. An eight-frame mosaic showing the temporal evolution of the P-Q complex in SL9. All images have been resampled to the observational conditions of the 30 March 1994 image; each frame has a width of ~90,000 km and a height of ~30,000 km. All of the images were taken with the WFPC2 in planetary mode, except that the 1 July 1993 image was taken with WFPC1 in planetary mode and the 17 May 1994 image was taken with WFPC2 in wide-field mode. Between January 1994 and March 1994 fragment P2 clearly became resolvable as two separate objects, indicating that a fragmentation event occurred sometime earlier. From the relative motions of Q1 and Q2, we estimated that these two fragments split from each other in April 1993. The inner comae around the brighter fragments remained circularly symmetric until ~2 weeks before impact into Jupiter, at which time the comae became highly elongated along the Jupiter-SL9 direction. The coma around fragment P1 was flatter than the comae around the brighter fragments, and this object became undetectable after its coma dissipated. Similarly P2b also disappeared. The brightening near the bottom of the 24 June 1994 image is due to a bright star whose effect was not completely removed by our processing. The brightening to the left of the 20 July 1994 image is due to scattered light from Jupiter.

mination of that fraction requires assumptions about the coma profile in the unresolved region.

Applying an iterative deconvolution technique, which assumes that the coma becomes completely flat in a 3 × 3 pixel region centered on the brightest pixel (*1*), we found that the brighter fragments have maximum effective diameters of ~2 to 4 km, assuming a geometric albedo of 4%. If the ρ^{-1} power law (ρ is the projected distance from the fragment) of the observed outer coma tailward profiles (compare with Fig. 3) is extended inward to the peak pixel, and if this extension is assumed to give the actual coma contribution at the peak pixel, the derived fragment diameter is reduced to ~70% of the value derived from the flat-coma deconvolution (for example, the diameter for fragment G would be ~3 km instead of 4 km). If a similar extrapolation is done by using a $\rho^{-1.33}$ power law, which gives a good fit to the circularly symmetric region, the coma contribution at the peak pixel actually exceeds the observed value. The noise in the observed intensity at the peak pixel corresponds to an equivalent diameter of ~1 to 2 km, so that it would be very easy to hide an object of this size within the comae of SL9.

A more sophisticated deconvolution technique, in which the nucleus (fragment) is modeled as a quasi-Gaussian and the coma brightness is modeled as either a quasi-Gaussian or a power law distribution, and allowing the nucleus and coma light distributions to be nonconcentric, was applied to the 1994 data (*13*). This analysis suggests that (i) the larger fragments have diameters of ~4 km assuming a geometric albedo of 4% and (ii) the fit is generally improved by adding a few companion fragments, whose diameters are also relatively large (~1 to 2 km). Attempts to fit the images by using only a coma brightness distribution generally produced significantly poorer residuals than fits that used both a coma and a relatively large fragment.

Both of the deconvolution techniques depend on assumptions about the coma brightness distribution, but as Fig. 3 illustrates, any extrapolation into the unresolved region is suspect. We conclude only that the larger fragments may have been a few kilometers in diameter, but that smaller values cannot be ruled out. The finding that there are multiple large fragments near the centers of each coma must be considered tentative.

The relative intensities for all of the SL9 fragments from the May 1994 observations are listed in Table 2, along with the relative diameters and impact energies of the fragments delivered to Jupiter, assuming that the diameter of the fragment is proportional to the square root of the intensity and that the energy is proportional to the cube of the diameter. Observations by the HST of the plumes and impact sites on Jupiter (*14*) indicate at least a gross correlation between the relative brightness of a fragment before impact and the magnitude of the impact phenomena, but there are several noteworthy exceptions. Fragment A produced much bigger ejecta features on Jupiter than its brightness indicated it would, whereas the Q fragments did the opposite. Generally, the off-train fragments produced smaller ejecta patterns than their brightness would predict. It seems plausible that the off-train fragments were inherently more fragile than the on-train fragments, if the former were the result of fragmentation after the breakup of the SL9 parent body, but the strength of the impacting body might not be very important in determining the magnitude of the impact phenomena. If the off-train fragments had relatively more dust (for example, because they were "younger"), that might explain why use of their observed intensities systematically overestimates their masses relative to the on-train fragments.

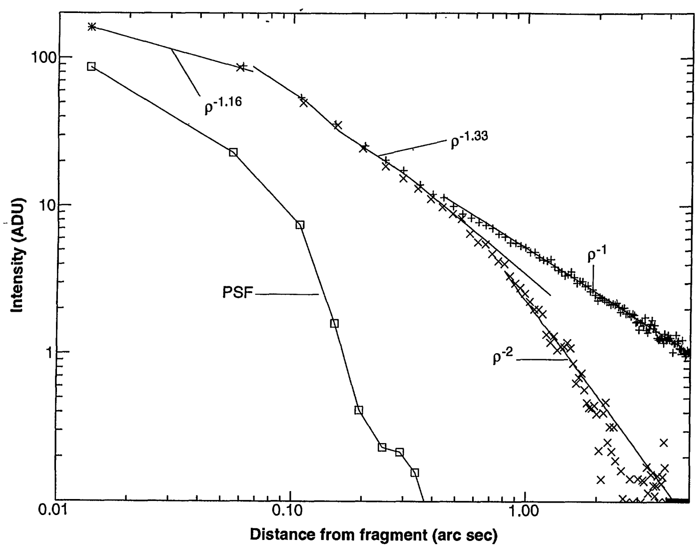

Fig. 3. Azimuthally averaged spatial brightness profiles are shown for one of the well-isolated fragments (G1) observed on 25 January 1994. The profiles for most of the other fragments are similar. The data in two 90° quadrants, whose central axes are approximately perpendicular to the line connecting the fragments, were used to construct the profiles. For one of the profiles (+) the points are on the tailward side of the line connecting the fragments, and for the other profile (x) the points are on the opposite side. A constant background level, the estimated residual sky signal, was subtracted from all pixel intensities. The error bars (not shown) on the observed profiles are approximately the same size as the plotting symbols for points within ~2 arc sec of the fragment and become slightly larger with increasing distance from the fragment. At the time of these observations, 1 arc sec projected to 3920 km at SL9. Also plotted are radial surface brightness profiles for various power-law brightness distributions (where ρ is the projected distance from the fragment). The observed SL9 profiles cannot be fit by a single power law over the entire range of distances covered. A model point spread function (PSF) computed for the position of the fragment, and whose intensity corresponds to the upper limit on the fragment magnitude, is also shown (□). ADU, analog-to-digital unit. See the text for further discussion.

Color of the Inner Coma

During January 1994 we took images through two different filters (F702W and

Table 2. Relative intensity, size, and energy ratios for SL9. The letter designation for each fragment is given first followed by the number designation in parentheses. The intensities (Int) are relative values for each fragment as measured in a 3 × 3 pixel box centered on the brightest pixel from the 17 May 1994 HST images. The relative sizes can be translated into approximate upper limits for the diameters (in kilometers) by multiplying by 1.4. Impact class refers to designations given to the impact sites by Hammel *et al.* (*14*). Those impact sites having the most spectacular visual appearance are in class 1, whereas sites that could not be detected in the HST images fell into class 4. See Hammel *et al.* (*14*) for further details. KE, kinetic energy.

ID	Int	Size	KE	Rank	Impact class
A (21)	1.0	1.0	1.0	17	2a
B (20)	1.5	1.2	1.8	14*	3
C (19)	2.2	1.5	3.2	12	2a
D (18)	1.0	1.0	1.0	16	3
E (17)	4.2	2.0	8.6	8	2a
F (16)	2.3	1.5	3.5	11*	4
G2 (15b)	0.33	0.58	0.19	21*	4
G1 (15a)	8.2	2.9	24	2	1
H (14)	4.9	2.2	11	5	2a
K (12)	7.3	2.7	20	3	1
L (11)	6.1	2.5	15	4	1
N (9)	1.0	1.0	1.0	15*	3
P2 (8b)	1.8	1.4	2.5	13*	4
P1 (8a)	0.38	0.61	0.23	20*	4
Q2 (7b)	4.8	2.2	10	6*	3
Q1 (7a)	8.6	2.9	25	1	2b
R (6)	3.3	1.8	5.9	9	2b
S (5)	4.3	2.1	9.1	7	2c
T (4)	0.21	0.46	0.099	22*	4
U (3)	0.42	0.65	0.28	19*	4
V (2)	0.95	0.97	0.92	18*	4
W (1)	3.0	1.7	5.1	10	2c

*These are the off-train fragments.

F555W) of fragments F, G, and H to measure the color of the dust in the part of the coma that is inaccessible from other telescopes. Color was obtained as the ratio of the spatial brightness profiles for each filter. In all cases, this brightness ratio (F702W/F555W) was between 1.5 and 2, and there was no obvious systematic variation as a function of nucleocentric distance from the peak pixel out to ~1.5 arc sec from the peak. We also performed circular aperture photometry (summing the flux in apertures of various radii) and transformed the derived magnitudes into standard Landolt-Cousins V and R magnitudes for comparison with color data obtained by one of us (K.J.M.) with the University of Hawaii 2.2-m telescope on Mauna Kea in mid-January 1994. The HST data yield $V - R = 0.40$ with an uncertainty (due primarily to the uncertainty in transforming the magnitudes as measured by the HST to the standard system) of ~0.15 for each of the three fragments. Our ground-based data give $V - R = 0.419 \pm 0.072$, 0.445 ± 0.029, and 0.458 ± 0.034 for the F, G, and H fragments, respectively, with the use of an aperture of radius 0.8 arc sec. The sun has $V - R = 0.35$ (*15*), so the dust in the inner coma of SL9 is slightly redder than solar color, which is typical of cometary dust (*16*). Our $V - R$ colors are also consistent with those derived from ground-based observations by Cochran *et al.* (*17*), who point out that the SL9 $V - R$ and $B - V$ colors are inconsistent with the colors observed for Pholus (an outer solar system body that seems to be unique in its colors) and for type B, F, D, P, R, V, and A asteroids, but are consistent with the colors of the more common type C and S asteroids.

Spectroscopy

Spectroscopy of SL9 was performed on three different occasions (Table 1) with the Faint Object Spectrograph (FOS). We were primarily searching for the hydroxyl radical (OH), which has been established as a tracer of water (H_2O) ice in comets and is the strongest emission in cometary spectra observed at heliocentric distances near 1 AU. We did not detect any emission in the OH [0,0] band near 3090 Å (the strongest band in the $A^2\Sigma$–$X^2\Pi$ system), either in the first two observations, centered near fragment Q1, or in the last observation, of the G1· fragment. From the model described earlier (*1*), the derived upper limits (3σ, where σ is the standard deviation) on the H_2O production rates are $\sim 1 \times 10^{27}$ to 2×10^{27} molecules per second (= 3 to 6 kg s^{-1}). Averaging all of the data together reduces the upper limit slightly to a number similar to the upper limit derived from ground-based observations of OH (*18*).

This null result does not necessarily mean that SL9 was derived from an asteroid (that is, a relatively ice-poor object). At SL9's heliocentric distance (~5.4 AU) an isothermal blackbody would have a temperature of ~120 K, at which temperature the sublimation rate of H_2O would be many orders of magnitude below our sensitivity limit. For a nonrotating nucleus, or one whose rotation axis is pointing near the sun, the subsolar temperature can approach ~170 K, and the sublimation rate averaged over the entire surface of the object is $\sim 10^{15}$ molecules per centimeter squared per second. In this case, one nonrotating nucleus having a diameter of ~5 to 6 km, and completely coated with ice, would produce H_2O at a rate equal to our upper limit. Thus, detectable amounts of OH would have been produced by means of sublimation from the remaining fragments only if they were very large and had a special rotational configuration.

Because small icy grains are likely to be much warmer than a blackbody at the same heliocentric distance (due to their inability to radiate at long wavelengths efficiently), significant H_2O production might also come from the grains near SL9. A total mass of icy grains in our field of view of $\sim 10^9$ g is required to produce enough OH to be detected with HST (*19*). On the basis of our imaging observations of the dust, the estimated dust mass in the FOS field of view was $\sim 4 \times 10^8$ g, indicating that it was not unreasonable to search for OH.

Although OH was not detected, strong Mg^+ emission at 2800 Å was observed at fragment G during an outburst on 14 July 1994 (Fig. 4). Approximately 18 min after the Mg^+ outburst, the continuum spectrum also changed dramatically, increasing by more than a factor of 3 at long wavelengths over an 8-min period, and then relaxing back to the quiescent level less than 20 min after the start of the outburst. At shorter wavelengths the changes were less pronounced (that is, the continuum became redder during the outburst).

If the Mg^+ was created by means of ion sputtering of dust, then one would also expect H_2O to be produced if the dust was coated with ice (*20*). The two lines in the Mg^+ doublet are partially resolved in the HST spectrum, indicating that the emission was strongly peaked within a spatial region of ~1000 km. Because OH is not produced directly from the sputtering, it would be created during the subsequent photolysis of H_2O and, consequently, would have a very broad spatial distribution. The OH emission would then perhaps be too diffuse to be detectable. We also note that neutral Mg was not detected, although resonance transition of neutral Mg was in our bandpass. Maybe the mechanism responsible for the outburst preferentially produces ionized species, offering another possible explanation why neutral OH was not detected. (The strong ultraviolet band of OH^+ was outside of our bandpass.)

The Mg^+ and continuum outbursts might have been due to the charging and subsequent bursting of small grains as the

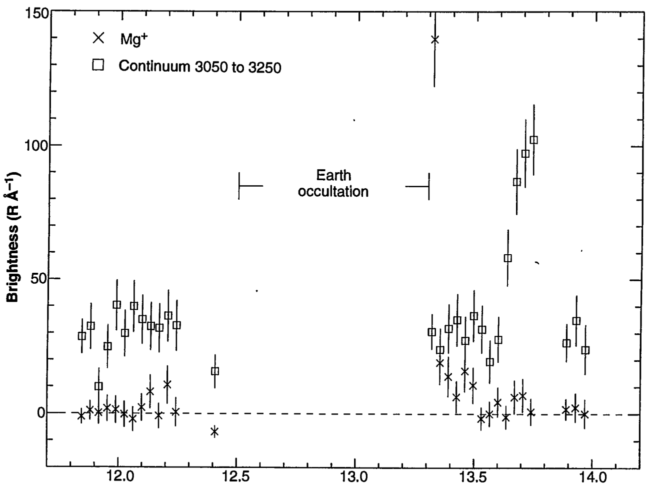

Fig. 4. Temporal evolution of the Mg^+ emission near 2800 Å and the continuum emission in the range of 3050 to 3250 Å. For the first 2-min exposure at the beginning of the second orbit the Mg^+ emission was very strong; this emission was essentially undetectable at other times. The emission cannot be telluric (that is, it must be associated with SL9) for the following reasons: (i) if the telluric emission were this strong it would have been seen in many other HST observations, but it is not; (ii) there was also a dramatic change in the continuum, indicating that something was happening at SL9; and (iii) the Mg^+ doublet was partially resolved into two separate lines, which would not be seen for a telluric emission filling the aperture. Shortly after the appearance and disappearance of the Mg^+ emission, the continuum became significantly reddened; the level near 3100 Å rose by at least a factor of 3, whereas the level below 2600 Å showed little change. These spectral outbursts may be associated with SL9's penetration of the jovian magnetopause. The spectra covered the wavelength range of 2222 to 3277 Å, and the effective aperture size was 3.7 arc sec (parallel to dispersion) by 1.2 arc sec (perpendicular to dispersion), which projected to 13,700 km by 4430 km at SL9. The error bars are $\pm 1\sigma$. The continuum emission was multiplied by 100 for clarity. The rayleigh (R) is a unit of column brightness that is commonly used in planetary astronomy and is 4π times the specific intensity (1 R = 10^6 photons cm^{-2} s^{-1}). UT, universal time.

comet penetrated into Jupiter's magnetosphere (*21*). At the time of these observations the comet was 3.8×10^6 km away from Jupiter, close to the magnetopause (*22*). The electrostatic potential on the surface of a dust grain due to electron bombardment is proportional to the electron temperature of the surrounding plasma, which increases by a factor of 100 in passing from interplanetary space into the jovian magnetosphere. If the grains are small enough and relatively fluffy, the self-repulsion of the surface charges will exceed the tensile strength and tear apart the grains. Dessler and Hill (*21*) estimated that cometary grains as large as 1 mm might suffer disruption in the jovian magnetosphere.

Other typical cometary emissions lying within our bandpass include those from CS and CO_2^+, but neither was observed. The parents of these species (that is, the ices in the nucleus from which the species are derived) are thought to be CS_2 and CO_2, both of which are much more volatile than H_2O. Thus, one might expect outgassing from these species even at 5 AU, if their sublimation temperatures in the comet (where there is a mixture of various ices) were similar to those in the pure state. Again, however, the many uncertainties involved in estimating the sublimation behavior of cometary ices in SL9 preclude the use of our null result to place meaningful limits on the size or nature of SL9.

Summary

The HST investigations do not provide definitive answers regarding the nature of SL9. No "typical" cometary emissions were observed spectroscopically, but due to sensitivity limitations, these results do not rule out the possibility that SL9 had a cometary composition. Perhaps the best evidence that SL9 was a comet was the existence of a persistent, circularly symmetric coma around each fragment, possibly indicating continuous dust production. However, the distinction between comets and asteroids is not always clear, especially for objects that formed in the trans-jovian region of the solar nebula. For such objects, including members of the outer portions of the asteroid belt, the volatile mass fraction may be intermediate between those of the more familiar examples of comets and asteroids, thus rendering futile any attempt to force SL9 into a specific category.

The question of the fragment sizes is also unresolved. Deconvolution analyses of the HST images suggest that the larger fragments of SL9 could have been as big as ~3 to 4 km in diameter, but significantly smaller values are also possible. Some of the fragments clearly continued to break up well after the tidal disruption of the parent body, further emphasizing the fragile nature of SL9. These disruptions indicate that a single, relatively large, solid body was at the center of each coma, as opposed to a swarm of thousands of much smaller objects. Despite the low tensile strengths of the fragments, most of the large ones appear to have maintained their structural integrity up until ~10 hours before their entry into Jupiter's atmosphere, at which time there were no more HST observations.

REFERENCES AND NOTES

1. H. A. Weaver *et al.*, *Science* **263**, 787 (1994).
2. The Wide Field Planetary Camera 2 (WFPC2) consists of three wide-field mode charge-coupled devices (CCDs) having 0.0996 arc sec pixel^{-1} and one planetary mode CCD having 0.0455 arc sec pixel^{-1}. The point spread function (PSF) of the planetary mode has a full-width at half-maximum of ~0.070 arc sec, which projects to 250 km at a geocentric distance of 5 astronomical units (AU). During the HST observations of SL9, the geocentric distance varied from 4.4 to 5.5 AU. Virtually all of our observations were made through the F702W filter, which is similar to the standard *R* band and has an effective wavelength of 6931 Å, but we also made some observations in January 1994 through the F555W filter, which is similar to the standard *V* band and has an effective wavelength of 5475 Å, in order to measure the $V - R$ color in the inner coma near several fragments.
3. Of the 39 orbits devoted to imaging of the comet, four were awarded to an independent team led by T. W. Rettig. Two images were taken during each orbit with exposure times of either 800 or 1000 s, depending on the acquisition time required in that orbit. Because cosmic rays, stars, and galaxies littered the images during the required long exposure times, we generally used two orbits to acquire four images of the same field in order to remove this contamination.
4. P. Chodas assisted with these calculations.
5. D. Jewitt and N. Trentham, *Int. Astron. Union Circ. 5999* (1994).
6. Intensity variations of ~20% in the comet can be due solely to changes in the phase angle and geocentric distance, rather than to intrinsic changes in the comet. After attempting to correct for these effects, we find, for example, that the core brightness (defined as the total flux in a 3 × 3 pixel square centered on the peak pixel) of fragment G decreased ~50% from January 1994 to July 1994, whereas the core brightness for fragment S was essentially unchanged over the same interval. A more detailed discussion of the temporal evolution of SL9 is deferred to a future publication.
7. If the velocities were too large, the dust cloud would be dispersed too rapidly. During the period of the HST observations, the amount of dust within ~2000 km of the fragment remained fairly steady, but the amount of dust at larger distances decreased dramatically with time. For example, the surface brightness at ~20,000 km into the tail decreased by a factor of ~4 between 1 July 1993 and 24 January 1994. As discussed later in this article, there may have been a continuous, low-level production of dust, which could explain the steady inner coma. However, there was also probably a large release of dust associated with the fragmentation of SL9's parent body. Small dust particles from this latter event would eventually be lost to the system because of outflow, which might explain the decrease in the coma brightness at large nucleocentric distances, whereas large dust particles would dissipate much more slowly. Subsequent fragmentation events would serve as perturbations to any steady-state production of dust.
8. Z. Sekanina, P. W. Chodas, D. K. Yeomans, *Astron. Astrophys.* **289**, 607 (1994). These researchers argued that steady-state production of dust was not possible in SL9 for two reasons: (i) A rapidly rotating tail ray was not observed during late March 1993, and (ii) a persistent dust feature located to the east-southeast of the train was not observed during April to July 1993. However, such features would be difficult to detect if the dust production rates and dust velocities were very small.
9. In calculating dust production rates, we assume that there is isotropic production at the nucleus of spherical dust grains having radii of 1 μm, densities of 1 g cm^{-3}, and a geometric albedo of 4%, and we assume that all grains are moving radially outward with a velocity of 0.1 km s^{-1}. There is significant uncertainty associated with each of these latter assumptions, but the largest uncertainty probably is in the velocity. An empirical relation for the dust velocity derived from coma halo measurements made by N. T. Bobrovnikoff [*Astron. J.* **59**, 357 (1954)] gives ~0.2 km s^{-1} at SL9's heliocentric distance. However, it has been argued [A. H. Delsemme, in *Comets*, L. L. Wilkening, Ed. (Univ. of Arizona Press, Tucson, AZ, 1982), pp. 85–130] that this relation actually applies to the gas velocity and not to that of the dust. If the rapid falloff of the coma brightness profile on one side of the SL9 train at a distance of ~10,000 km from the nucleus can be associated with an apex due to solar radiation pressure [compare L. V. Wallace and F. D. Miller, *Astron. J.* **63**, 213 (1958)], then the dust outflow velocity might be significantly less than 0.1 km s^{-1}. Pending a more detailed analysis of the observed dust distribution in SL9, we admit that our choice could be wrong by a factor of 10 or more. Our derived production rates scale linearly with the velocity.
10. With the data reported in K. J. Meech, M. J. S. Belton, B. E. A. Mueller, M. W. Dicksion, H. R. Li [*Astron. J.* **106**, 1222 (1993)], we derive a dust production rate of ~50 kg s^{-1} for comet P/Schwassmann-Wachmann 1 at a heliocentric distance of 5.8 AU. Using completely different assumptions about the grain size distribution, M. Fulle [*Nature* **359**, 42 (1990)] derived a dust production rate of ~1000 kg s^{-1}. Both values are appropriate for the so-called quiescent phase of this highly variable comet.
11. For P/Halley we derived a dust production rate of ~3 kg s^{-1} using the visual magnitude observed through a 2.5-arc sec radius aperture by S. Wyckoff, R. M. Wagner, P. A. Wehinger, D. G. Schleicher, and M. C. Festou [*Nature* **316**, 241 (1985)].
12. P. Weissman, personal communication.
13. Z. Sekanina, in a paper presented at the Hypervelocity Impact Symposium, Sante Fe, NM, (1994); *Int. Astron. Union Circ. 6020* (1994).
14. H. B. Hammel *et al.*, *Science* **267**, 1288 (1995).
15. C. W. Allen, *Astrophysical Quantities* (Athlone, London, ed. 3, 1976), p. 162. The relations defined by A. Landolt [*Astron. J.* **88**, 439 (1983)] were used to transform from the Johnson photometric system into the Landolt-Cousins system.
16. D. Jewitt and K. J. Meech, *Astrophys. J.* **310**, 937 (1986).
17. A. L. Cochran *et al.*, *Icarus*, in press.
18. A. L. Cochran *et al.*, *ibid.* These ground-based observations used a long-slit spectrograph so that many fragments could be observed simultaneously. Their quoted upper limits for gas production refer to the total values summed over many fragments, whereas the HST results refer to gas production from a single fragment.
19. We assume spherical grains with a radius of 1 μm, a density of 1 g cm^{-3}, an infrared emissivity of 0.35, and an emissivity at visual wavelengths of 1. Under these conditions the grain temperature is ~155 K and the sublimation rate is ~10^{14} molecules cm^{-2} s^{-1}.
20. W. L. Brown, L. J. Lanzerotti, R. E. Johnson, *Science* **218**, 525 (1982).
21. A. J. Dessler and T. W. Hill, *Geophys. Res. Lett.* **21**, 1043 (1994).
22. The exact location of the magnetopause depends on the level of solar activity and the jovicentric latitude. According to M. H. Acuna, K. W. Behannon, J. E. P. Connerney [in *Physics of the Jovian Magnetosphere*, A. J. Dessler, Ed. (Cambridge Univ. Press, Cambridge, 1983), pp. 1–50], the magnetopause location should lie in the range of ~3×10^6 to 7×10^6 km from Jupiter.

23. This work is based on observations with the National Aeronautics and Space Administration (NASA)–European Space Agency HST obtained at the Space Telescope Science Institute (STScI), which is operated by the Association of Universities for Research in Astronomy under NASA contract NAS5-26555. Support for this work was provided by NASA through grant numbers GO-5021.01-92A and GO-5624.01-93A from the STScI. We thank K. Jones for his assistance in reducing and analyzing the data, the STScI support staff for their work in implementing our program, and R. Williams, the STScI director, for allocating some of his director's discretionary time for our program. The HST project scientist, D. Leckrone, deserves special thanks for the support he provided during all aspects of the HST comet-Jupiter campaign. We are also thankful for support provided by the HST program scientist at NASA headquarters, E. Weiler. We acknowledge helpful conversations with A. J. Dessler and M. A. McGrath regarding the interpretation of the spectral outbursts. Finally, we thank all of our colleagues who participated in the HST comet-Jupiter campaign for making this experience fun, as well as enriching.

HST Imaging of Atmospheric Phenomena Created by the Impact of Comet Shoemaker-Levy 9

H. B. Hammel, R. F. Beebe, A. P. Ingersoll, G. S. Orton, J. R. Mills, A. A. Simon, P. Chodas, J. T. Clarke, E. De Jong, T. E. Dowling, J. Harrington, L. F. Huber, E. Karkoschka, C. M. Santori, A. Toigo, D. Yeomans, R. A. West

Hubble Space Telescope (HST) images reveal major atmospheric changes created by the collision of comet Shoemaker-Levy 9 with Jupiter. Plumes rose to 3000 kilometers with ejection velocities on the order of 10 kilometers second^{-1}; some plumes were visible in the shadow of Jupiter before rising into sunlight. During some impacts, the incoming bolide may have been detected. Impact times were on average about 8 minutes later than predicted. Atmospheric waves were seen with a wave front speed of 454 ± 20 meters second^{-1}. The HST images reveal impact site evolution and record the overall change in Jupiter's appearance as a result of the bombardment.

The collision of comet Shoemaker-Levy 9 with Jupiter provided an unprecedented opportunity to study the reaction of a thick planetary atmosphere to a rapid deposition of energy. Predictions ranged from no observable effects (*1*) to major atmospheric disturbances, including explosive plumes (*2, 3*) and atmospheric waves (*4, 5*). Our atmospheric imaging program received 39 Hubble Space Telescope (HST) orbits to use the Wide Field and Planetary Camera 2 (WFPC2) for observations of dynamical effects in Jupiter's atmosphere from the event. We scheduled most of the orbits for the week of impacts, reserving six orbits for pre-impact characterization and nine orbits for observations of post-impact evolution. We selected a set of key filters (Table 1) and cycled through them as often as possible (*6, 7*). To our delight, many effects on Jupiter's atmosphere were detectable with HST.

H. B. Hammel, J. R. Mills, T. E. Dowling, J. Harrington, and C. M. Santori are in the Department of Earth, Atmospheric, and Planetary Sciences, Massachusetts Institute of Technology, Cambridge, MA 02139, USA. R. F. Beebe, A. A. Simon, and L. F. Huber are in the Astronomy Department, New Mexico State University, Las Cruces, NM 88003, USA. A. P. Ingersoll and A. Toigo are in the Division of Geology and Planetary Science, California Institute of Technology, Pasadena, CA 91125, USA. G. S. Orton, P. Chodas, E. De Jong, D. Yeomans, and R. A. West are at Jet Propulsion Laboratory, California Institute of Technology, Pasadena, CA 91109, USA. J. T. Clarke is in the Department of Atmospheric and Oceanic Sciences, University of Michigan, Ann Arbor, MI 48109, USA. E. Karkoschka is at Lunar and Planetary Laboratory, University of Arizona, Tucson, AZ 85721, USA.

Impact Sites

We detected impact sites for 15 fragments; five fragments left no discernible disturbance. Figure 1 shows a series of projections of several fresh (less than 3 hours old) impact sites as they would appear to an observer directly overhead. Table 2 gives our measurements of latitudes and longitudes of the detected sites, along with the predicted impact times and locations (*8*). From the observed longitudes, we inferred impact times. We also classified each impact site by its apparent size in the first image after impact; these classes agree roughly with pre-impact fragment brightnesses (*9*).

For the largest fresh impact sites, we noted a consistent morphology: a prominent circular ring and sometimes a faint ring inside the main ring concentric with it but visible mainly on the northwest side of the ring center, a small triangle with its apex near the ring center and its base to the southeast, a larger crescent-shaped ejecta also to the southeast, and rays in the crescent that seemed to emanate from a point slightly to the southeast of the ring center. In the methane absorption band, impact debris was brighter than the normal jovian clouds, suggesting that it was at a relatively high altitude, above most of the methane gas. At other wavelengths, the impact debris appeared darker than the normal jovian clouds. We discuss here the asymmetric ejecta; waves are discussed in more detail below.

Ballistic ejecta pattern. The outer edge of the crescent formed by impact G (the G impact crescent) is 13,000 km from the ring center (which presumably marks the point of maximum energy release). The speed of the ejecta must have been at least 17 km s^{-1}, assuming ballistic particles launched at an elevation angle of 45° (the predicted elevation angle of both the bolide and the ejected plume). The crescent shape of the ejecta suggests that the range of elevation angles is small. Assuming this range was centered around 45°, the vertical component of the velocity is slightly greater than 12 km s^{-1}. At this speed, particles will travel for 17 min before returning to their initial ejection level, during which time they will rise to a height of 3200 km. The latter is close to the maximum height of the G plume determined from HST images, and this time is consistent with observed plume durations (Figs. 2 and 3) (Table 3). At any other elevation angle, the required velocity would be higher; for example, material ejected straight up at the same velocity of 17 km s^{-1} would reach 6400 km (higher than observed). The material is not highly collimated in azimuth: the crescent extends at least 180° around the impact site.

The azimuth of the symmetry axis of the ejecta pattern indicates how long the material was in flight, because the planet rotated during that time. The fragments entered the atmosphere at an elevation angle of 45°, with the azimuth angle 16° counterclockwise from south; models of oblique impacts (*3*) predict the ejection of material back along this same trajectory. To a good approximation, the vertical component of the rotation vector tells us how far the planet rotated while the material was in flight. The rotation increases the azimuth angle by $\Omega t \sin\phi$, where Ω is the angular velocity of the planet, t is the time of flight, and ϕ is the planetocentric latitude. For t = 17 min, corresponding to a height of 3200 km, the rotation angle is 7°, giving a total azimuth angle from south of 23°. However, the observed azimuth is 35° ± 5°, implying that the material was in flight for 45 min; this conclusion holds also for the material near the impact point, because the azimuth of the small triangle is at least 35°. Ejected material may slide along the top of the atmosphere following its oblique high-speed reentry. If friction with the underlying layer is low, the rotation is the same as if the